Journal of
Applied Physics
ARTICLE
pubs.aip.org/aip/jap

MBE growth, structural, optical, and thermal properties of AlBN

Cite as: J. Appl. Phys. **139**, 063101 (2026); doi: 10.1063/5.0307890
Submitted: 17 October 2025 · Accepted: 13 January 2026 ·
Published Online: 9 February 2026

View Online Export Citation CrossMark

Chandrashekhar Savant,[1,a)] Saurabh Vishwakarma,[2] Thai-Son Nguyen,[1] Len van Deurzen,[3] Joongwon Lee,[4] Gustavo Alvarez,[5] Hsin Wei S. Huang,[4] Kazuki Nomoto,[4] Zhiting Tian,[5] Farhan Rana,[4] David J. Smith,[6] Huili Grace Xing,[1,4,7] and Debdeep Jena[1,3,4,7]

AFFILIATIONS

[1] Department of Materials Science and Engineering, Cornell University, Ithaca, New York 14853, USA
[2] School for Engineering of Matter, Transport and Energy, Arizona State University, Tempe, Arizona 85287, USA
[3] School of Applied and Engineering Physics, Cornell University, Ithaca, New York 14853, USA
[4] School of Electrical and Computer Engineering, Cornell University, Ithaca, New York 14853, USA
[5] Sibley School of Mechanical and Aerospace Engineering, Cornell University, Ithaca, New York 14853, USA
[6] Department of Physics, Arizona State University, Tempe, Arizona 85287, USA
[7] Kavli Institute at Cornell for Nanoscale Science, Cornell University, Ithaca, New York 14853, USA

[a)] **Author to whom correspondence should be addressed:** cps259@cornell.edu

ABSTRACT

We report plasma-assisted molecular beam epitaxial growth of AlBN thin films on a nitrided c-plane Al_2O_3 substrate. The AlBN film epitaxially grows in rotational alignment with an out-of-plane/in-plane directions of AlBN $[000\bar{1}]/[10\bar{1}0] \parallel$ AlN nucleation layer $[000\bar{1}]/[10\bar{1}0] \parallel Al_2O_3$ $[0001]/[11\bar{2}0]$. The B composition of the AlBN layer is varied from 0% to 15% by varying the growth temperature, exploiting the reaction rate-controlled growth mechanism. X-ray diffraction and high-resolution transmission electron microscopy are used to determine the structural properties as a function of boron composition. A monotonic decrease in the *c*-lattice constant and a non-monotonic change in the *a*-lattice constant are observed with an increase in the B content in AlBN films grown on nitrided sapphire. While the control AlN film showed a bandgap of 6.1 eV, the AlBN films with ∼15% boron showed a bandgap of 5.9 eV. The AlBN films with 15% B exhibit a fivefold increase in the nonlinear second-harmonic generation intensity compared to AlN. AlBN films exhibit higher thermal conductivity than AlScN films with comparable alloy compositions, and at equal or smaller thicknesses. The findings indicate several opportunities for AlBN films in applications of deep UV optoelectronics, nonlinear photonics, and high-power electronics devices, especially in high-voltage and high-temperature environments.

I. INTRODUCTION

Wurtzite group-III nitrides have been widely investigated over the last three decades, leading to breakthroughs in devices for solid-state lighting, acoustoelectric filters, and high-power electronics.[1–5] Among the well-established Al, Ga, and In-nitride materials, aluminum nitride (AlN) has the widest bandgap (∼6.1–6.2 eV) and appreciable intrinsic second-order optical nonlinearity with piezoelectric coefficients of ∼4–7 pm/V and a dielectric constant of ∼8.4.[4–7] Consequently, AlN plays a pivotal role in deep ultraviolet (UV) optoelectronics, nonlinear photonics, and acoustic and RF power electronic devices.[4,5,7,8] The performance of many of these devices is limited by the intrinsic material properties and partly by the structural quality and epitaxial registry of the layers.

In the last few years, it has been discovered that alloying isovalent group-III elements, such as B, Sc, and Y, into AlN imparts ferroelectricity and enhances the high-K dielectric constant and nonlinear optical properties.[9–15] Alloying a smaller lattice constant material, wurtzite BN, to AlN can retain or increase its ultrawide bandgap (UWBG) while enhancing the functionalities.[8,11,12,14,16,17] Compared to the alloys AlScN, AlYN, AlLaN, and AlLuN, AlBN retains the UWBG of AlN since the bandgap of BN in all phases (5.96 eV for h-BN, 6.4 eV for c-BN, and 6.84 eV for wurtzite-BN)[8,14,18,19] is larger than that of ScN, YN, LaN, LuN, etc.[20–26] Since the B atom is lighter than Al, Sc, Y, La, the thermal conductivity of AlBN is expected to be higher than AlScN, AlYN, and AlLaN alternatives. Furthermore, AlBN is more suitable for extreme temperature, voltage, and radiation environments as it is expected to be more resistant to oxidation compared to AlScN and other transition/rare-earth metal-based nitrides.[17,27,28]

AlBN is of interest not only for high-power electronics but also for deep UV photonics and nonlinear optoelectronic applications.[8,14,18] Recently, ferroelectricity and high-K dielectric properties have been discovered in AlBN films grown by sputtering[11,29] and MBE.[12,16] Epitaxial growth of AlBN on GaN has recently led to the realization of high-K AlBN barrier GaN HEMT using polarization-induced 2D electron gas (2DEG) at the AlBN/GaN heterojunction.[30] Although significant efforts have been recently dedicated to studying the high-K dielectric and ferroelectric properties of AlBN films for integration in RF and memory applications, reports on its epitaxial growth and structural, thermal, and optical properties remain scarce. In particular, prior studies have reported AlBN growth using ammonia-MBE, BBr_3 precursor-based PAMBE, and energetic neutral atom beam lithography and epitaxy (ENABLE)-MBE techniques, but these approaches suffered from limited B incorporation, phase segregation, and impurity contamination.[31–33]

Prior studies of sputter-deposited AlBN films have reported X-ray diffraction (XRD) ω 002 rocking curve (RC) full width at half maximum (FWHM) of $\sim 10^3$ to 10^4 arc sec, a slight reduction in the optical bandgap from 6.1 eV for AlN to 5.8 eV for AlBN with ∼11% B, a decrease in the refractive index, and an enhancement of nonlinear optical properties of AlBN films with B incorporation.[11,14] Owing to its ultrahigh vacuum nature, elemental purity of sources, and low substrate damage from the low kinetic energy of evaporated molecular beams, molecular beam epitaxy (MBE) exploits unique growth dynamics to yield films of high crystal quality and high epitaxial registry to the underlying substrate.[34] The structural, thermal conductivity, and optical properties of the epitaxial AlBN films grown by nitrogen plasma MBE are of high interest.

Here, we report the plasma-assisted MBE growth of wurtzite AlBN films with 0%–15.3% B concentration on nitrided sapphire substrates using a nitrogen plasma source and aluminum and boron effusion cells. We report the effect of MBE growth parameters, such as B cell temperature and substrate temperature, on the B content of AlBN. We identify the crystal structure and epitaxial registry of the AlBN films with AlN nucleation layers and the Al_2O_3 substrate, and measure their structural, thermal, and optical properties.

II. EXPERIMENTAL

All growths in this study were performed using a Veeco® GenXplor nitrogen plasma-assisted molecular beam epitaxy (MBE) system. The idle base pressure of the growth chamber was 10^{-9} Torr. A boron source of 6N purity and an aluminum source of 6N purity were obtained from United Mineral & Chemical Corp (UMC). The boron source material was loaded in a conical pyrolytic graphite liner, placed inside a conical tungsten crucible, and evaporated using a ∼2100 °C rated high-temperature effusion cell. An aluminum source was loaded in a pyrolytic boron nitride (PBN) crucible and evaporated using an effusion cell. A Veeco® RF UNI-Bulb plasma source was used to supply active nitrogen species into the growth chamber using 6N5 purity nitrogen gas. During growth, the chamber pressure was approximately 2×10^{-5} Torr. The nitrogen plasma was struck at 500 W RF power and an N_2 flow rate of 3 sccm. The N_2 flow rate was decreased to 1.95 sccm used during the sapphire substrate nitridation performed at 400 W RF power and the growth of AlBN films performed at 200 W RF power. A KSA Instruments reflection high-energy electron diffraction (RHEED) apparatus with a Staib electron gun operating at 14.5 kV and 1.45 A was used to monitor the growth surface *in situ*. The RHEED diffraction images were acquired along $[1\bar{1}00]$ and $[11\bar{2}0]$ zone axes of the sapphire substrate during the MBE growth.

The surface morphology of the AlBN films was analyzed by atomic force microscopy (AFM) performed in the tapping mode using an Asylum Research® Cypher ES system. XRD reciprocal space map (RSM) and ϕ scans of asymmetric Bragg reflections were collected using a Panalytical Empyrean® diffractometer with a 1.5406 Å Cu Kα x-ray source operated at 45 kV, 40 mA to characterize the phase, crystal structure, and orientation. The chemical composition of the AlBN films was analyzed with X-ray photoelectron spectroscopy (XPS) using a Scienta-Omicron-ESCA-2SR instrument equipped with a 1486.6 eV Al Kα x-ray source. Adventitious carbon and native oxide were removed from the sample surface using an Ar^+ ion beam. High-resolution Al2p, B1s, N1s, and C1s core-level X-ray photoelectron spectra were collected using a hemispherical analyzer (HCA) detector with a pass energy of 58.7 eV.

Cross-sectional samples for high-resolution transmission electron microscopy (HR-TEM) were prepared by focused ion beam (FIB) milling using a Thermo Fisher® Helios 5UX dual-beam instrument with initial thinning done at 30 keV and further thinning at 5 keV and 2 keV. A Philips-FEI CM200 HR-TEM operated at 200 kV was used to record the high-resolution TEM images. Electron energy loss spectroscopy (EELS) measurement was performed for elemental composition mapping. Wet etching in KOH was performed to test the polarity of the as-grown AlBN film grown on the nitrided sapphire substrate. The optical bandgap of the AlBN films was determined using ultraviolet-visible spectroscopy carried out using the Agilent Cary 5000 UV-Vis-NIR spectrophotometer.

The nonlinear optical properties of AlBN films were investigated using transmission second-harmonic generation (SHG) measurements. A Yb-fiber-based laser with 1032 nm wavelength, 150 fs pulse width, and 100 MHz repetition rate was used as a pump. The pump was focused onto a 50 μm spot on the AlBN film at a 45° incidence angle. A polarizer was used to control the polarization of the pump, while an analyzer was rotated to measure the polarization of the induced second-harmonic light. The intensity of the second-harmonic light was measured using a spectrometer paired with a charge-coupled device (CCD) camera.

Thermal conductivity (κ) measurements were carried out with frequency domain thermoreflectance (FDTR), an optical pump–probe technique utilizing two separate continuous wave (CW) lasers. A 488 nm pump laser beam passes through an electro-optic modulator (EOM) driven by a function generator modulated from 1 kHz to 10 MHz and provides the modulated heat source. A lock-in amplifier records the amplitude and phase response of the reflected 532 nm probe beam to the thermal wave, and these quantities are related to the properties of the multilayer sample.[35] The ideal lock-in amplifier measures the fundamental harmonic components of the probe signal at the modulation frequency and rejects all other components.[35] The weighted sample frequency response is obtained by solving the heat diffusion equation for a Gaussian heat source (the pump beam) impinging on a multilayer stack of materials and weighting the resulting temperature distribution at the top surface by the Gaussian intensity distribution of the probe beam.[35] The details can be found elsewhere.[36,37] FDTR has been previously applied to study homoepitaxial AlN, pulsed laser deposited h-BN, and MBE-grown AlScN.[38–40]

III. RESULTS AND DISCUSSION

Figure 1(a) schematically shows the layer heterostructure grown by MBE for this study. The surface of a c-plane sapphire substrate was nitrided at a substrate thermocouple temperature of 250 °C for 1.5 h, using active nitrogen species generated at 400 W RF power at a 1.95 sccm nitrogen flow rate. The Al_2O_3 substrate was first nitrided to form an AlN nucleation layer. Epitaxial wurtzite-phase AlBN films were then grown on the nitrided sapphire substrates under nitrogen-rich conditions and at different substrate temperatures, as described later. A control AlN film was also grown on nitrided sapphire without supplying boron flux.

Figure 1(b) shows the evolution of RHEED patterns collected during the MBE growth of AlBN/nitrided sapphire heterostructures along two zone axes of the Al_2O_3 substrate, i.e., along the Al_2O_3 $[11\bar{2}0]$ zone axis (ZA), at a 0° in-plane ϕ rotation of the substrate, and along Al_2O_3 $[1\bar{1}00]$ ZA, at a 30° in-plane ϕ rotation of the substrate. The nucleation of an AlN layer was observed during the plasma nitridation of the Al_2O_3 substrate, as indicated by the streaky RHEED diffraction pattern of wurtzite AlN with AlN $[1\bar{1}00]$ ZA $\|$ Al_2O_3 $[11\bar{2}0]$ ZA, at $\phi_{\text{substrate}} = 0°$ and AlN $[11\bar{2}0]$ ZA $\|$ Al_2O_3 $[1\bar{1}00]$ ZA at $\phi_{\text{substrate}} = 30°$. The switching between $[1\bar{1}00]$ and $[11\bar{2}0]$ zone axes during plasma nitridation of Al_2O_3 indicates that AlN nucleates at 30° basal in-plane rotation alignment with the Al_2O_3 substrate. Similar to the epitaxial growth of GaN on sapphire, the AlN layer forms at a 30° in-plane rotation with respect to the sapphire lattice to minimize the misfit strain since the O-atomic plane of Al_2O_3 is symmetrically matched with the Al-atomic plane in AlN.[41,42]

During the subsequent AlBN film growth, a spotty RHEED pattern is observed, as shown in the top Fig. 1(b) for the 8% B containing AlBN film. The observed RHEED diffraction spots for the AlBN film along the $[1\bar{1}00]$ ZA and $[11\bar{2}0]$ ZA indicate Bragg reflections corresponding to first-order 1 × 1 reconstruction for the wurtzite phase structure.[43,44] Throughout the growth of the AlBN film, this wurtzite phase RHEED pattern persists. A similar spotty wurtzite RHEED pattern was observed for all AlBN in this study, suggesting a three-dimensional growth mode under nitrogen-rich growth conditions required for B incorporation in AlBN.[44–46]

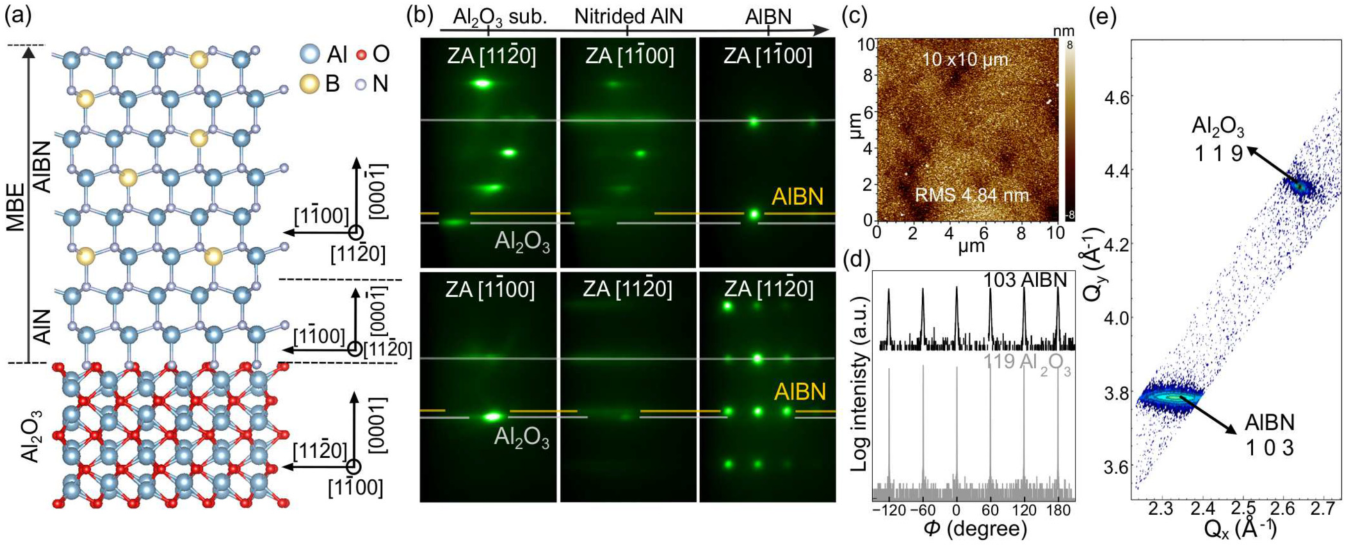

FIG. 1. (a) Schematic of the AlBN/nitrided sapphire heterostructure, with nitrogen-polar AlBN films. (b) RHEED evolution during growth along the Al_2O_3 $[11\bar{2}0]$ zone axis at $\phi_{\text{substrate}} = 0°$ (top row) and the Al_2O_3 $[1\bar{1}00]$ zone axis at $\phi_{\text{substrate}} = 30°$ (bottom row) showing epitaxial registry of MBE-grown films with a 30° rotation of hexagonal in-plane basal planes of AlBN and AlN with that of the Al_2O_3 substrate. (c) $10 \times 10\,\mu m^2$ AFM micrograph of a ∼250 nm AlBN film with 8% B. (d) Symmetric skew ϕ scans of AlBN 103, AlN 103, and Al_2O_3 119 Bragg reflections indicating epitaxial registry of AlBN on a sapphire substrate. (e) XRD-RSM map showing AlBN 103 and Al_2O_3 119 Bragg reflections for a sample with 8% B.

Figure 1(b) shows RHEED images collected at $\phi_{\text{substrate}} = 0°$ (top row) and $\phi_{\text{substrate}} = 30°$ (bottom row) during the growth showing AlBN $[1\bar{1}00]$ ZA ∥ AlN $[1\bar{1}00]$ ZA ∥ Al_2O_3 $[11\bar{2}0]$ ZA and AlBN $[11\bar{2}0]$ ZA ∥ AlN $[11\bar{2}0]$ ZA ∥ Al_2O_3 $[1\bar{1}00]$ ZA. This indicates that the AlBN films are epitaxially aligned with the AlN nucleation layer, exhibiting zero degrees of in-plane rotational misalignment. In contrast, both nitride layers grow at a 30° basal in-plane rotational alignment with the Al_2O_3 substrate since the crystallographic $[11\bar{2}0]$ and $[1\bar{1}00]$ axes in a hexagonal basal plane are separated by 30°.

Figure 1(c) shows a $10 \times 10\,\mu m^2$ AFM micrograph of a 200-nm-thick ∼8% B containing an AlBN film/nitrided sapphire sample exhibiting ∼4.8 nm rms roughness. Comparable surface roughness and surface morphology were observed for all the AlBN/nitrided sapphire samples grown in this study. The MBE-grown AlBN film was found to etch in wet KOH, leaving behind pyramids. This suggests that the as-grown AlBN films on a nitrided sapphire substrate are nitrogen-polar as illustrated in Fig. 1(a).[9,12,47,48] A similar nitrogen-polar growth of wurtzite AlN and GaN films has been reported previously after the nitridation of a sapphire substrate or after the removal of native oxide from an N-polar AlN substrate.[49–52]

Skew-geometry phi-scans of asymmetric AlBN 103 and Al_2O_3 119 Bragg reflections for a sample containing 8% B are shown in Fig. 1(d). Six peaks at the same $\phi_{\text{substrate}}$ positions indicate the sixfold symmetry and the epitaxial registry of the AlBN film with an Al_2O_3 substrate. The asymmetric AlBN 103 and Al_2O_3 119 peaks originate from diffraction from $\{10\bar{1}3\}$ AlBN, and $\{11\bar{2}9\}$ Al_2O_3 sets of crystallographic planes with in-plane projection normals along $\langle 10\bar{1}0\rangle$ AlBN and $\langle 11\bar{2}0\rangle$ Al_2O_3 crystallographic directions. AlBN 103 and Al_2O_3 119 peaks coincide at similar in-plane ϕ rotational angles, i.e., at $\phi_{\text{substrate}} = 0°$, $+/-60°$, $+/-120°$, 180° suggesting that the AlBN $\langle 10\bar{1}0\rangle$ crystallographic axes ∥ Al_2O_3 $\langle 11\bar{2}0\rangle$ crystallographic axes. The AlBN film grows epitaxially with out-of-plane/in-plane directions of AlBN $[000\bar{1}]/[10\bar{1}0]$ ∥ Al_2O_3 $[0001]/[11\bar{2}0]$, i.e., with a 30° basal in-plane rotational alignment between AlBN and Al_2O_3. Similar sixfold symmetry and epitaxial registry were also observed for other samples.

Figure 1(e) shows the measured X-ray diffraction reciprocal space map (XRD-RSM) peaks showing 103 AlBN and 119 Al_2O_3 Bragg reflections, implying that AlBN is of the wurtzite phase and the hexagonal phase of the Al_2O_3 substrate. The XRD-RSM maps shown in Fig. 1(e) were collected at a fixed $\phi_{\text{substrate}} = 0°$ with the x-ray beam ∥ Al_2O_3 $[11\bar{2}L]$. Only the allowed Bragg reflections corresponding to AlBN $10\bar{1}L$ and Al_2O_3 $11\bar{2}L$ were observed at this fixed ϕ rotation, whereas other Bragg peaks, such as AlBN $11\bar{2}L$, were absent, indicating that the AlBN crystals only grew in an epitaxial relationship with Al_2O_3, without apparent misoriented grains. XRD-RSM maps of other AlBN/nitrided sapphire samples used in this study (not shown) have a similar diffraction pattern, indicating a similar crystal structure and epitaxial registry.

It has been reported that the B incorporation in the AlBN films is primarily controlled by the MBE substrate temperature rather than by the supplied B flux species, as the AlBN films grow in a reaction rate-controlled regime rather than a mass transport-controlled regime.[16] Thus, to obtain AlBN films of different boron compositions, we used substrate growth temperatures of 600, 750, and 950 °C while keeping the other growth parameters the same. Since N exhibits a thermodynamic preference to bond to Al rather than B, a nitrogen-rich growth condition with a III/V ratio of ∼0.9 was used to grow the AlBN films in this study.[46] The effusion cell fluxes of boron and aluminum follow Arrhenius behaviors with an activation energy of ∼5.17 and ∼3.28 eV/atom, comparable to reported values.[16,53–55] A boron flux of $\sim 2.6 \times 10^{-8}$ Torr and an aluminum flux of $\sim 2.1 \times 10^{-7}$ Torr were obtained by keeping the B cell temperature at 1850 °C, and Al cell temperature at 1208 °C, while active nitrogen species flux of 2.6×10^{-7} Torr was obtained using 200 W RF power and 1.95 sccm nitrogen flow rate.

The composition of the AlBN films as a function of substrate temperature is plotted in Fig. 2. As the AlBN growth temperature increased from 600 to 750 to 950 °C, the B content in the AlBN films decreased from 15.3% to 8% to 3.1%. The BN phase diagram indicates that the wurtzite phase of binary BN is stable at temperatures below ∼1000–1500 K, while the layered hexagonal and cubic phases are stable at higher temperatures.[8,56,57] Low substrate temperatures promote B incorporation in a wurtzite form in AlBN films, possibly hindering conversion to hexagonal (or cubic) BN as B% increases in crystalline wurtzite AlBN films.[57]

Figure 3(a) shows the XRD symmetric 2θ–ω spectra of the control AlN film sample and the AlBN film samples grown at different substrate temperatures on the nitrided sapphire substrate. The XRD peaks corresponding to 002 Bragg reflections of wurtzite AlBN and 006 Bragg reflections of Al_2O_3 are observed, suggesting that the AlBN films grow along the $\langle 0001\rangle$ crystallographic axis on the *c*-plane sapphire substrate. With increasing boron content in the AlBN films, the 002 Bragg peak shifts to a higher 2θ–ω value, suggesting a decrease in the *c* lattice parameter. This is expected due to the smaller size of the unit cell lattice constant of wurtzite BN ($c_{BN} = 4.20$ Å) compared to that of the wurtzite AlN ($c_{AlN} = 4.99$ Å).[8] The XRD ω 002 rocking curve (RC) full-width

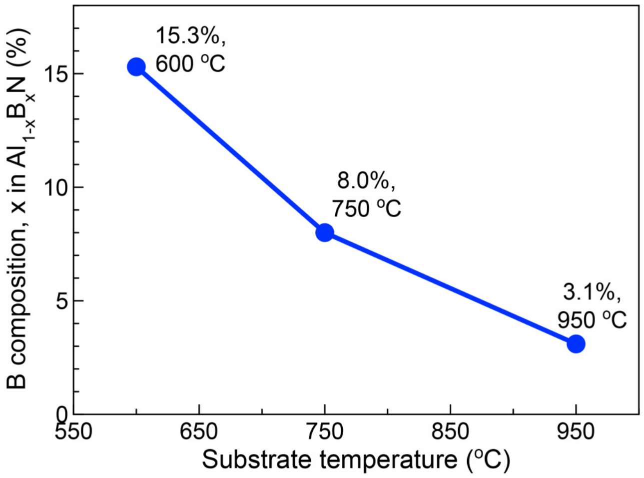

FIG. 2. Effect of MBE substrate growth temperature on the boron composition of AlBN films grown on nitrided sapphire.

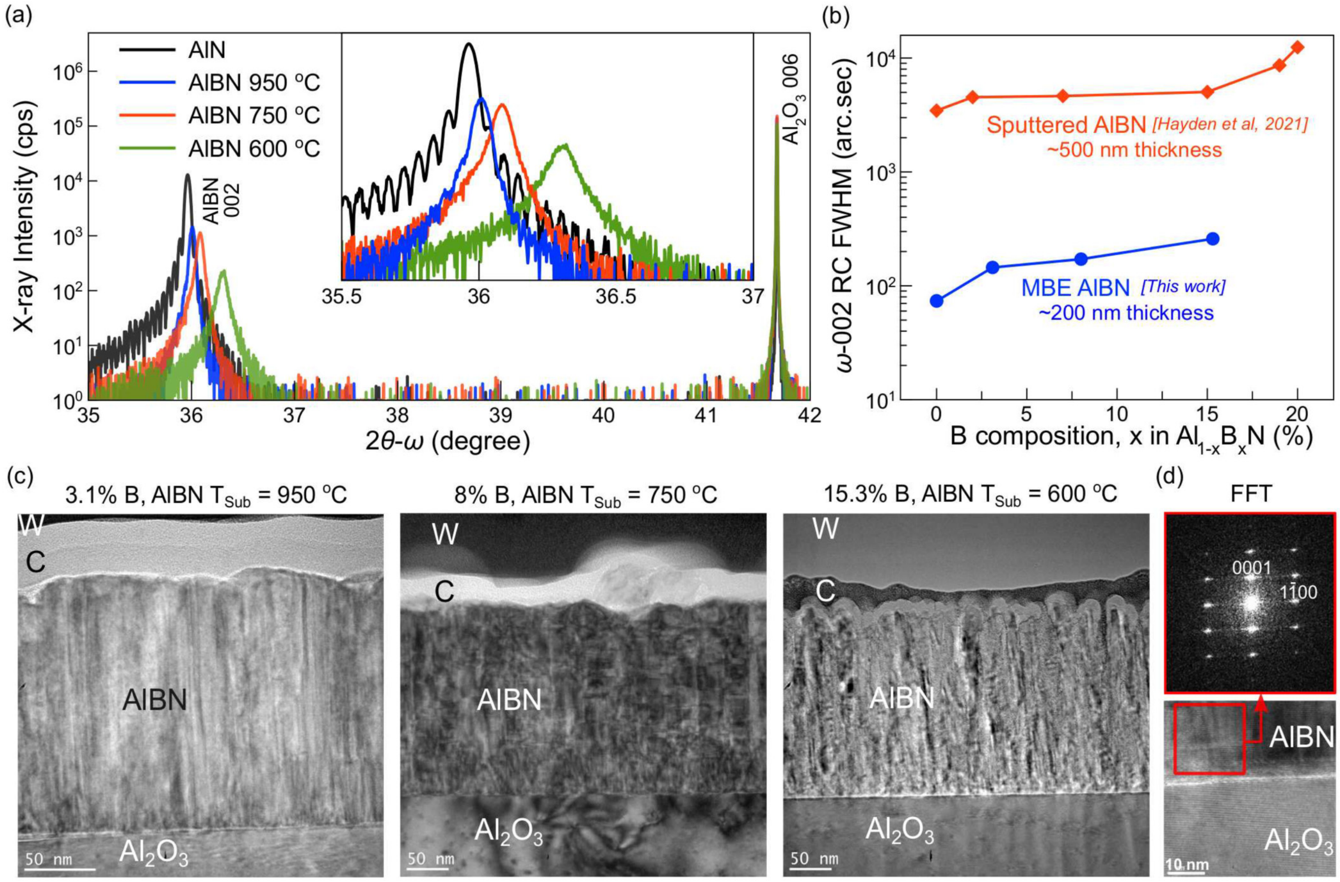

FIG. 3. (a) XRD symmetric 2θ–ω curves of AlBN films grown at different substrate temperatures on a nitrided sapphire substrate. (b) XRD ω 002 rocking curve FWHM values for MBE-grown AlBN films and for the sputter-deposited AlBN films as a function of B composition. (c) TEM micrographs of AlBN films showing columnar grain growth and decreasing film quality with decreasing substrate temperature, increasing B%. (d) TEM-FFT along the [11$\bar{2}$0] zone axis showing the wurtzite phase of AlBN films with 8% B.

half maximum (FWHM) values for MBE-grown AlBN films and the sputter-deposited AlBN films[11] as a function of B composition are shown in Fig. 3(b). The control AlN film grown by MBE showed a ω 002 RC FWHM value of ∼74 arc sec, which increases to ∼144 to 260 arc sec with increasing boron content from 3% to 15%. The ω-002 RC FWHM values of ∼200 nm thick MBE-grown AlBN films are at least one order of magnitude lower than those of ∼500 nm thick sputter-deposited films, suggesting a large crystalline size of MBE-grown AlBN films.

Figure 3(c) shows TEM micrographs of AlBN films with 3.1%, 8%, and 15.3% B. The AlBN films exhibit columnar crystal morphology, possibly arising from a three-dimensional Volmer–Weber growth mode common in nitrogen-rich growth conditions. The crystallinity of the AlBN films decreases with decreasing growth temperature and increasing B content, as observed in HR-TEM micrographs and an increase in the XRD ω-002 RC FWHM values. Figure 3(d) shows a HRTEM micrograph (bottom) of an AlBN/nitrided sapphire film sample with 8% B and a Fast Fourier transform (FFT) of the AlBN film region enclosing the heterostructure as marked by the square red box. The FFT shows ⟨0002⟩ spots in the [11$\bar{2}$0] projection as confirmed by the simulated diffraction patterns (not shown) for wurtzite phase AlBN along [11$\bar{2}$0] ZA. This confirms the wurtzite phase of the AlBN film, with no apparent signs of secondary phases observed in the TEM micrographs and FFT patterns of AlBN films. From the TEM FFT patterns, the *c* lattice parameters of 4.98, 4.98, and 4.94 Å were calculated for AlBN films with 3.1%, 8%, and 15.3% B, respectively.

Additional HR-TEM, FFT, and EELS analyses (see Figs. S1–S3 in the supplementary material) further confirm that the defect density increases markedly with higher B incorporation in the AlBN films. The 3.1% B sample grown at 950 °C exhibits highly crystalline, epitaxial columnar grains with a smooth top surface and only minor tilting of columnar grains. At 8% B, the film remains epitaxial but develops more crystalline defects, including inversion domain boundaries and basal stacking faults. In contrast, the 15.3% B sample grown at 600 °C was quite defective away from the Al_2O_3 substrate, with grain misalignments approaching ~5° and even extensive gaps between the highly tilted columnar grains; EELS mapping also confirmed non-uniform B and N distributions in this film. Overall, these results demonstrate that higher B incorporation in MBE-grown AlBN films leads to significant degradation in film quality, consistent with prior reports on MOVPE-grown AlBN films.[58–61]

Figure 4(a) illustrates the crystal structure of a wurtzite AlBN cell with a "ball and stick" model showing the c and a axis lattice parameters measured from XRD AlBN 002 and 103 Bragg reflections. Figure 4(b) shows the measured values as a function of the B composition. With increasing B content, c-lattice parameter decreases monotonically from the $c_{\mathrm{AlN}} = 4.99$ Å of the control AlN to $c_{\mathrm{AlBN}} = 4.98$, 4.97, and 4.94 Å for AlBN with 3.1%, 8% and 15.3% B, respectively. The in-plane a-parameter changes non-monotonically with B content, initially increasing from $a_{\mathrm{AlN}} = 3.103$ Å to $a_{\mathrm{AlBN}} = 3.116$ Å for 3.1% B and decreasing to $a_{\mathrm{AlBN}} = 3.091$ Å for 15.3% B.

B incorporation in the AlN lattice causes a decrease in the c lattice parameter. The predicted c-parameter of 4.20 Å for wurtzite BN[8] is smaller than 4.99 Å of AlN owing to a smaller size of B compared to Al. The c-parameter of AlBN films is expected to decrease with increasing B content. The substitution of B in the wurtzite AlN lattice leads to local distortion in the AlN_4 tetrahedra, causing deviations in tetrahedral bond angles from the ideal 109.4°.[14,62] The vertical bonds in the ideal tetrahedra of AlN_4 can deflect away from the c-axis by as much as 13° for ~22% B in AlBN.[14,62] Thus, an increase in the in-plane a-parameter of AlN with up to ~3.1% B incorporation could be due to distortion of tetrahedral geometry toward the trigonal planar or hexagonal structure.[14,62] The a-parameter decreases with increasing B content of the AlBN films from ~3% to ~15.3% since the expected a-parameter 2.54 Å for the wurtzite BN is smaller than 3.103 Å of AlN.[8] Figure 4(b) implies that, though AlBN cannot be lattice matched to relaxed c-plane GaN, AlBN films with ~10–11% B can be lattice matched to relaxed c-plane AlN.

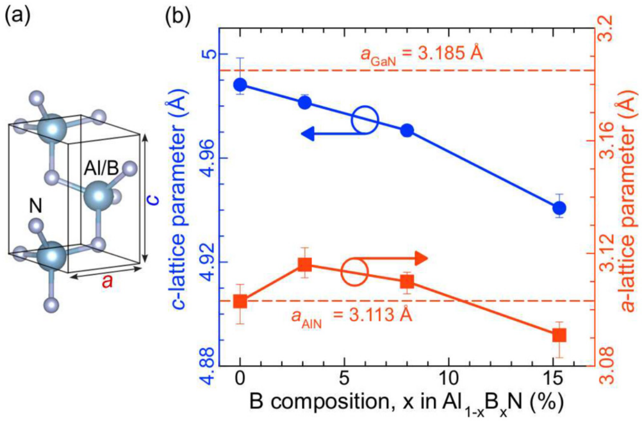

FIG. 4. Structural properties of AlBN films grown on a nitrided sapphire substrate. (a) Ball and stick crystal structure model of wurtzite AlBN films showing c and a axes, orientations, and lattice parameters. (b) c-axis and a-axis lattice parameters of wurtzite AlBN films grown on nitrided sapphire as a function of B content, x%.

The nitrogen-polar surfaces of wurtzite semiconductors, such as AlN, GaN, and InN, etch at higher rates than metal-polar surfaces in KOH or H_3PO_4 leaving behind pyramids with $\{10\bar{1}\bar{1}\}$ planes as these are energetically stable because of a smaller number of bonds through these planes.[9,47,48,63] The SEM micrographs taken after KOH etching of the AlBN/nitrided sapphire sample indicate that the AlBN film was etched, leaving hexagonal pyramids. This suggests that the as-grown AlBN film on a nitrided sapphire substrate is nitrogen-polar, and the growth direction of AlBN films is $\{000\bar{1}\}$ crystallographic axis ∥ Al_2O_3 {0001} crystallographic axis.

Optical absorption spectra of the AlBN/nitrided sapphire samples were measured using ultraviolet-visible absorption spectroscopy. Figure 5(a) shows the optical bandgap of energies

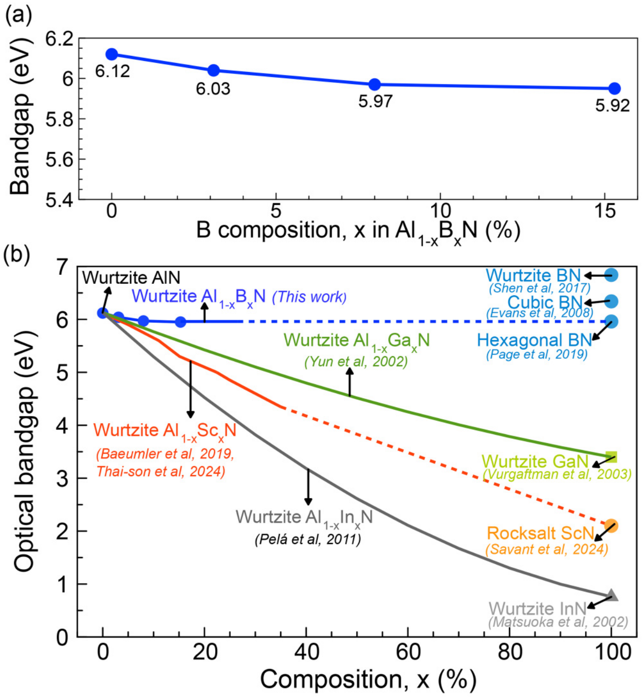

FIG. 5. (a) Optical bandgap of AlBN films as a function of different B composition. (b) Optical bandgap vs composition of ternary Al(B/Sc/Ga/In)N nitrides and that of binary AlN, BN, ScN, GaN, and InN nitrides.[18,42,64–71] The wurtzite phase of AlBN and AlScN is reported to be stable up to 26% B and ~30–35% Sc.[72–74] Dashed lines for $Al_{1-x}B_xN$ films from $x = 0.26-1$ and $Al_{1-x}Sc_xN$ films from $x = \sim 0.35-1$ indicate the metastable nature of the wurtzite phase in this composition ranges. Compared to Sc, Ga, and In, incorporating B retains the ultrawide bandgap of AlN. Reproduced with permission from Yun *et al.*, J. Appl. Phys. **92**, 4837–4839 (2002). Copyright 2002 AIP Publishing LLC. Reproduced with permission from Pelá *et al.*, Appl. Phys. Lett. **98**, 151907 (2011). Copyright 2011 AIP Publishing LLC. Reproduced with permission from Nguyen *et al.*, *2024 International Electron Devices Meeting (IEDM)* (IEEE, 2024), pp. 9.5.1–9.5.4. Copyright 2024 IEEE. From Baeumler *et al.*, J. Appl. Phys. **126**, 045715 (2019). Copyright 2019 Author(s), licensed under a Creative Commons Attribution (CC BY) License.

determined from a Tauc plot of $\sqrt{\alpha h\upsilon}$ vs photon energy, $h\upsilon$, where α is the absorption coefficient, h is Planck's constant, and υ is the photon frequency. The control AlN film exhibits an absorption edge of ∼6.1 eV, close to the reported values of 6.1–6.2 eV.[4,14] As shown in Fig. 5(a), the bandgap energy decreases with increasing B content from 6.1 eV for 0% B to 5.9 eV for ∼15% B containing AlBN films. Similar ultrawide bandgaps of AlBN films are also reported in the films deposited by sputtering, with a bandgap of ∼6.1 eV to 5.8 eV for 0%–11% B.[14] Figure 5(b) shows the optical bandgap of ternary Al(B/Sc/Ga/In)N nitrides plotted as a function of composition, and that of binary AlN, BN, ScN, GaN, and InN nitrides.[18,42,64–71] Like wurtzite AlN, BN is also an ultrawide bandgap semiconductor in all crystalline forms. The bandgaps are 6.4 eV for cubic BN, 5.98 eV for hexagonal BN, and 6.84 eV for wurtzite BN.[4,8,42] Therefore, incorporating B into the wurtzite AlN lattice retains an ultrawide bandgap.[8,14] On the other hand, the optical bandgaps of other binary group III nitrides are substantially lower than AlN, e.g., 3.4 eV for GaN, 0.76 eV for InN, 2.1–2.3 eV for ScN, 1.45 eV for YN, 0.82 eV for LaN, and 1.1 eV for LuN.[4,8,23,24,75] Thus, the optical bandgaps of ternary nitrides of AlN decrease with increasing substitution of Al with other group-III elements, such as Ga, In, Sc, Y, and La. The ultrawide bandgap of AlBN is expected to maintain a larger breakdown voltage than the other high-K, ferroelectric nitride alternative.

Figure 6 shows the polarization of the second harmonic generation (SHG) intensity of a 15% B-containing MBE-grown AlBN film sample compared to the control AlN film sample while illuminated by a s-polarized pump at 45° angle of incidence. The second-harmonic light is p-polarized, as expected from the symmetry of the wurtzite crystal. An enhancement of SHG intensity by ∼5 times for the MBE-grown AlBN film sample with 15% B is observed compared to the control AlN film sample. A similar enhancement in the SHG intensity was observed for sputter-deposited AlBN films, primarily attributed to the enhancement in piezoelectric d_{15} and d_{31} SHG coefficients.[14] B incorporation in AlN enhances its intrinsic second-order optical nonlinearity while retaining its ultrawide bandgap. Thus, AlBN has the potential to be a CMOS-compatible, nonlinear optical material for integrated photonic devices.

Figure 7(a) shows the thermal conductivity κ of ternary AlBN, AlScN,[40] AlGaN,[76–79] InGaN,[78–80] and InAlN[79–81] nitrides plotted

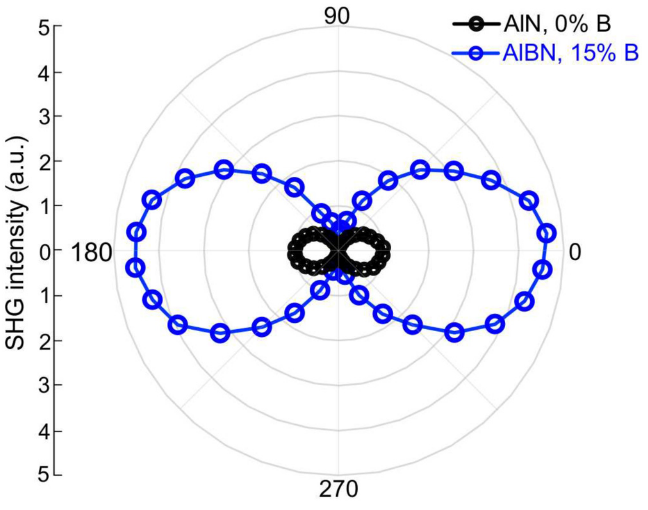

FIG. 6. Second-harmonic generation intensity plotted as a function of the analyzer angle, while illuminated with an s-polarized pump at 45° angle of incidence. The horizontal axis (0° and 180°) represents the p-polarization. SHG intensity is enhanced by ∼5 times for the AlBN film sample with 15% B compared to the AlN film sample.

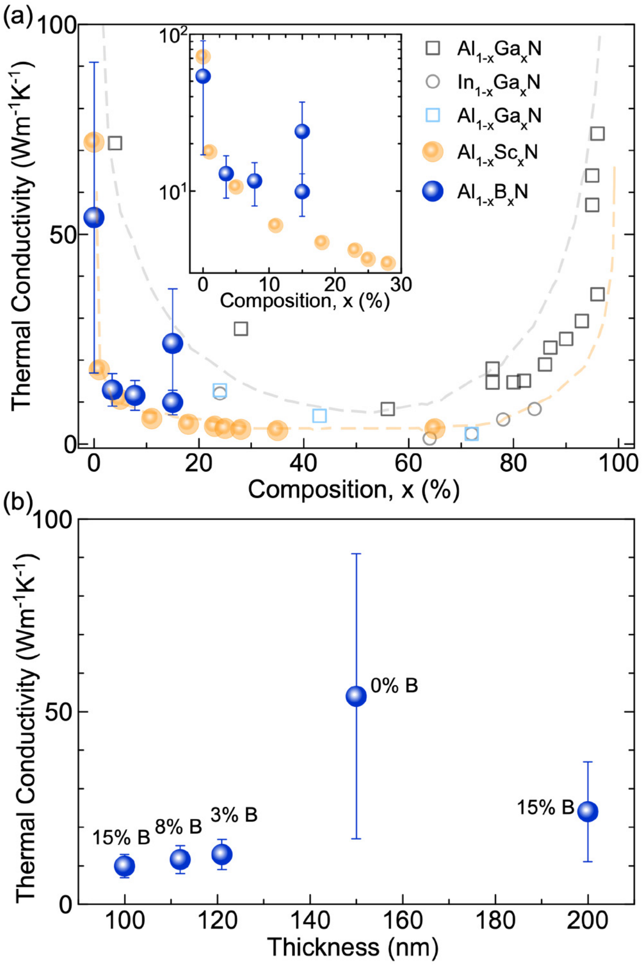

FIG. 7. (a) Thermal conductivity, κ, of ternary nitrides of AlBN, AlScN, AlGaN, InGaN, and InAlN plotted as a function of composition. Measured thermal conductivity of AlBN is plotted with the reported values of AlGaN, InGaN, InAlN, and AlScN for comparison.[40] As the B, Sc, Ga, and In concentrations increase, the typical alloy scattering behavior causes an abrupt reduction in κ, which AlBN also follows. The inset shows thermal conductivities of AlBN and AlScN at low alloying compositions. (b) Thermal conductivity (κ) plotted as a function of AlBN film thickness. From Alvarez *et al.*, Mater. Res. Lett. **11**, 1048–1054 (2023). Copyright 2023 Author(s), licensed under a Creative Commons Attribution (CC BY) License.

as a function of composition. The observed decline in thermal conductivity of AlBN with increasing B content due to alloying is consistent with previous experimental studies of various ternary nitride materials. The characteristic U-shape trend, in which small alloying concentrations cause a significant drop in κ, is illustrated in Fig. 7(a). This sharp decline is attributed to alloy-induced crystal lattice distortion, which enhances phonon-alloy scattering.[76,78]

The inset of Fig. 7(a) compares thermal conductivities of AlBN and AlScN at similar alloy compositions. At low alloy contents, AlBN shows thermal conductivities that are comparable to, and in some cases slightly higher than, those of AlScN when measured at similar or smaller thicknesses. For example, at 15% B, the κ of AlBN films is $24.0 \pm 13.0\,\mathrm{W\,m^{-1}\,K^{-1}}$ for 200 nm thickness and $9.90 \pm 3.00\,\mathrm{W\,m^{-1}\,K^{-1}}$ for 100 nm thickness. At 11% Sc, a 200 nm AlScN film has a κ of $6.03 \pm 0.74\,\mathrm{W\,m^{-1}\,K^{-1}}$.[40] This corresponds to a significant increase in the thermal conductivity for the 200 nm and 100 nm AlBN films relative to the 200 nm AlScN film. Another important factor is the size effect on κ, which arises when the phonon mean free path becomes comparable to the thin film thickness, leading to boundary scattering. As shown in Fig. 7(b), the κ of the 15% B in AlBN at 200 nm in thickness is larger than that of the 15% B containing AlBN at 100 nm, illustrating the reduction in boundary scattering with increased thickness. Preliminary results suggest that AlBN-based devices may offer comparable or slightly improved heat dissipation to AlScN. However, considering measurement uncertainties, further systematic studies across varied compositions and thicknesses are needed to fully explore the potential of this emerging material.

IV. CONCLUSION

In summary, we report the epitaxial growth and structural, thermal, and optical properties of wurtzite-AlBN films on nitrided c-Al_2O_3 substrates using MBE. AlBN films with a controlled 0 to 15.3% B composition are grown in a reaction rate-controlled growth regime. The AlBN film and the AlN nucleation layer grow in epitaxial registry and rotational alignment with the O-atomic planes of Al_2O_3. A monotonic decrease in the *c*-parameter and a non-monotonic change in the *a*-parameter are observed with increased B% in AlBN films. AlBN with ∼10%–11% B can be potentially lattice matched to AlN. UV-vis absorption spectra indicate 5.9 eV bandgap of the AlBN films with ∼15.3% boron. This decrease in bandgap on B incorporation in AlN is small compared to that reported for the incorporation of Ga, In, Sc, etc., in AlN. A ∼5 times enhancement of the nonlinear second-harmonic generation intensity is observed with B incorporation in AlN. AlBN films exhibit comparable or slightly higher thermal conductivity than AlScN films at comparable alloy compositions and smaller film thicknesses. These results provide a new understanding of the epitaxial growth of AlBN films with a controlled B composition by MBE and highlight the structural, thermal, and optical properties of AlBN films for applications in deep UV optoelectronics, nonlinear photonics, and high-power electronic devices.

SUPPLEMENTARY MATERIAL

See the supplementary material for the HR-TEM micrographs, FFT, and EELS element mapping data for MBE-grown AlBN films.

ACKNOWLEDGMENTS

This work was supported in part by the Ultra Materials for a Resilient Energy Grid (epitaxy and microscopy), an Energy Frontier Research Center funded by the U.S. Department of Energy, Office of Science, Basic Energy Sciences under Award No. DE-SC0021230 and in part by SUPREME, one of seven centers in JUMP 2.0, a Semiconductor Research Corporation (SRC) program sponsored by DARPA (characterization). The authors acknowledge the use of facilities within the John M. Cowley Center for High Resolution Electron Microscopy at Arizona State University, supported in part by NNCI-ECCS-1542160. The authors also acknowledge the use of the Cornell NanoScale Facility (CNF), a member of the National Nanotechnology Coordinated Infrastructure (NNCI), which is supported by the National Science Foundation (NSF Grant No. NNCI-2025233). This work used the Cornell Center for Materials Research (CCMR) Shared Facilities, funded through the NSF MRSEC program (DMR-1719875).

AUTHOR DECLARATIONS

Conflict of Interest

The authors have no conflicts to disclose.

Author Contributions

Chandrashekhar Savant: Conceptualization (lead); Data curation (lead); Formal analysis (lead); Investigation (lead); Methodology (lead); Validation (lead); Writing – original draft (lead); Writing – review & editing (lead). **Saurabh Vishwakarma:** Data curation (equal); Formal analysis (equal); Writing – review & editing (supporting). **Thai-Son Nguyen:** Data curation (equal); Formal analysis (equal); Writing – review & editing (supporting). **Len van Deurzen:** Data curation (supporting); Validation (supporting). **Joongwon Lee:** Data curation (equal); Formal analysis (equal); Software (supporting); Writing – original draft (supporting). **Gustavo Alvarez:** Data curation (equal); Writing – original draft (supporting). **Hsin Wei S. Huang:** Formal analysis (supporting). **Kazuki Nomoto:** Methodology (supporting); Validation (supporting). **Zhiting Tian:** Resources (supporting); Supervision (supporting). **Farhan Rana:** Resources (supporting); Supervision (supporting). **David J. Smith:** Resources (equal); Supervision (equal); Validation (supporting); Writing – original draft (supporting); Writing – review & editing (supporting). **Huili Grace Xing:** Funding acquisition (equal); Investigation (equal); Project administration (equal); Resources (equal); Supervision (equal). **Debdeep Jena:** Funding acquisition (lead); Project administration (lead); Resources (lead); Supervision (lead); Validation (equal); Writing – original draft (supporting); Writing – review & editing (supporting).

DATA AVAILABILITY

The data that support the findings of this study are available from the corresponding author upon reasonable request.

REFERENCES

[1] I. Akasaki, "Nobel lecture: Fascinated journeys into blue light," Rev. Mod. Phys. **87**, 1119–1131 (2015).

[2] H. Amano, "Nobel lecture: Growth of GaN on sapphire via low-temperature deposited buffer layer and realization of p-type GaN by Mg doping followed by low-energy electron beam irradiation," Rev. Mod. Phys. **87**, 1133–1138 (2015).

[3] S. Nakamura, "Nobel lecture: Background story of the invention of efficient blue InGaN light emitting diodes," Rev. Mod. Phys. **87**, 1139–1151 (2015).

[4] D. Jena, R. Page, J. Casamento, P. Dang, J. Singhal, Z. Zhang, J. Wright, G. Khalsa, Y. Cho, and H. G. Xing, "The new nitrides: Layered, ferroelectric, magnetic, metallic and superconducting nitrides to boost the GaN photonics and electronics eco-system," Jpn. J. Appl. Phys. **58**, SC0801 (2019).

[5] S. T. Haider, M. A. Shah, D.-G. Lee, and S. Hur, "A review of the recent applications of aluminum nitride-based piezoelectric devices," IEEE Access **11**, 58779–58795 (2023).

[6] M. Kneissl and J. Rass, *III-Nitride Ultraviolet Emitters: Technology and Applications* (Springer, 2015), Vol. 227.

[7] N. Li, C. P. Ho, S. Zhu, Y. H. Fu, Y. Zhu, and L. Y. T. Lee, "Aluminium nitride integrated photonics: A review," Nanophotonics **10**, 2347–2387 (2021).

[8] R. Kudrawiec and D. Hommel, "Bandgap engineering in III-nitrides with boron and group V elements: Toward applications in ultraviolet emitters," Appl. Phys. Rev. **7**, 041314 (2020).

[9] S. Fichtner, N. Wolff, F. Lofink, L. Kienle, and B. Wagner, "AlScN: A III-V semiconductor based ferroelectric," J. Appl. Phys. **125**, 114103 (2019).

[10] J. Casamento, H. Lee, T. Maeda, V. Gund, K. Nomoto, L. van Deurzen, W. Turner, P. Fay, S. Mu, C. G. Van de Walle *et al.*, "Epitaxial Sc$_x$Al$_{1-x}$N on GaN exhibits attractive high-K dielectric properties," Appl. Phys. Lett. **120**, 152901 (2022).

[11] J. Hayden, M. D. Hossain, Y. Xiong, K. Ferri, W. Zhu, M. V. Imperatore, N. Giebink, S. Trolier-McKinstry, I. Dabo, and J.-P. Maria, "Ferroelectricity in boron-substituted aluminum nitride thin films," Phys. Rev. Mater. **5**, 044412 (2021).

[12] C. Savant, V. Gund, K. Nomoto, T. Maeda, S. Jadhav, J. Lee, M. Ramesh, E. Kim, T.-S. Nguyen, Y.-H. Chen *et al.*, "Ferroelectric AlBN films by molecular beam epitaxy," Appl. Phys. Lett. **125**, 072902 (2024).

[13] D. Wang, S. Mondal, J. Liu, M. Hu, P. Wang, S. Yang, D. Wang, Y. Xiao, Y. Wu, T. Ma *et al.*, "Ferroelectric YAlN grown by molecular beam epitaxy," Appl. Phys. Lett. **123**, 033504 (2023).

[14] A. Suceava, J. Hayden, K. P. Kelley, Y. Xiong, B. Fazlioglu-Yalcin, I. Dabo, S. Trolier-McKinstry, J.-P. Maria, and V. Gopalan, "Enhancement of second-order optical nonlinearities and nanoscale periodic domain patterning in ferroelectric boron-substituted aluminum nitride thin films," Opt. Mater. Express **13**, 1522–1534 (2023).

[15] J. Liu, P.-L. Thériault, W. Wu, Q. Wen, S. Kéna-Cohen, M. Kira, and Z. Mi, "Ferroelectric AlScN as an extreme nonlinear quantum material beyond LiNbO$_3$," in *Quantum 2.0* (Optica Publishing Group, 2023), pp. QW3B–5.

[16] C. Savant, T.-S. Nguyen, S. Vishwakarma, J. Lee, A. Ithepalli, Y.-H. Chen, K. Nomoto, F. Rana, D. J. Smith, H. G. Xing *et al.*, "Epitaxial AlBN/β-Nb$_2$N ferroelectric/superconductor heterostructures," Phys. Status Solidi RRL **18**, 2400157 (2024).

[17] A. Earnshaw and N. N. Greenwood, *Chemistry of the Elements* (Butterworth-Heinemann, Oxford, 1997), Vol. 60.

[18] J.-X. Shen, D. Wickramaratne, and C. G. Van de Walle, "Band bowing and the direct-to-indirect crossover in random BAlN alloys," Phys. Rev. Mater. **1**, 065001 (2017).

[19] C. L. Milne, T. Biswas, and A. K. Singh, "Electronic properties of ultra-wide bandgap B$_x$Al$_{1-x}$N computed from first-principles simulations," Adv. Electron. Mater. **11**, 2400549 (2025).

[20] A. R. Smith, H. A. N. Al-Brithen, D. C. Ingram, and D. Gall, "Molecular beam epitaxy control of the structural, optical, and electronic properties of ScN (001)," J. Appl. Phys. **90**, 1809–1816 (2001).

[21] B. Saha, J. Acharya, T. D. Sands, and U. V. Waghmare, "Electronic structure, phonons, and thermal properties of ScN, ZrN, and HfN: A first-principles study," J. Appl. Phys. **107**, 033715 (2010).

[22] J. Casamento, K. Nomoto, T.-S. Nguyen, H. Lee, C. Savant, L. Li, A. Hickman, T. Maeda, Y.-T. Shao, J. Encomendero, V. Gund, T. Vasen, S. Afroz, D. Hannan, D. A. Muller, H. G. Xing, and D. Jena, "AlScN high electron mobility transistors: Integrating high piezoelectric, high K dielectric, and ferroelectric functionality," in *2023 IEEE BiCMOS and BCICTS* (IEEE, 2023), pp. 132–136.

[23] M. J. Winiarski and D. Kowalska, "Electronic structure of REN (RE = Sc, Y, La, and Lu) semiconductors by MBJLDA calculations," Mater. Res. Express **6**, 095910 (2019).

[24] M. J. Winiarski and D. A. Kowalska, "Crystal structure of rare earth and group III nitride alloys by ab initio calculations," Sci. Rep. **10**, 16414 (2020).

[25] P. Larson, W. R. L. Lambrecht, A. Chantis, and M. Van Schilfgaarde, "Electronic structure of rare-earth nitrides using the LSDA + U approach: Importance of allowing 4f orbitals to break the cubic crystal symmetry," Phys. Rev. B **75**, 045114 (2007).

[26] S. Leone, I. Streicher, M. Prescher, P. Straňák, and L. Kirste, "Metal-organic chemical vapor deposition of aluminum yttrium nitride," Phys. Status Solidi RRL **17**, 2300091 (2023).

[27] Y. Utsumi, T. Imai, and N. Fujimori, "Boron-aluminum nitride coating and method of producing same," U.S. patent 5,766,783 (16 June 1998).

[28] J. Casamento, H. G. Xing, and D. Jena, "Oxygen incorporation in the molecular beam epitaxy growth of Sc$_x$Ga$_{1-x}$N and Sc$_x$Al$_{1-x}$N," Phys. Status Solidi B **257**, 1900612 (2020).

[29] S. Calderon, J. Hayden, S. M. Baksa, W. Tzou, S. Trolier-McKinstry, I. Dabo, J.-P. Maria, and E. C. Dickey, "Atomic-scale polarization switching in wurtzite ferroelectrics," Science **380**, 1034–1038 (2023).

[30] C. Savant, T.-S. Nguyen, K. Nomoto, S. Vishwakarma, S. Ma, A. Dhar, Y.-H. Chen, J. Casamento, D. J. Smith, H. G. Xing *et al.*, "Epitaxial high-K barrier AlBN/GaN HEMTs," Appl. Phys. Lett. **126**, 112906 (2025).

[31] V. Gupta, C. Wamsley, M. Koch, and G. Wicks, "Molecular beam epitaxy growth of boron-containing nitrides," J. Vac. Sci. Technol. B **17**, 1246–1248 (1999).

[32] R. C. Cramer, "Extreme III-nitride alloys grown via plasma-assisted molecular beam epitaxy," Ph.D. thesis (University of California, Santa Barbara, 2019).

[33] T. L. Williamson, N. R. Weisse-Bernstein, and M. A. Hoffbauer, "Growth of ternary wurtzite BAlN and BGaN by ENABLE-MBE," Phys. Status Solidi C **11**, 462–465 (2014).

[34] W. Nunn, T. K. Truttmann, and B. Jalan, "A review of molecular-beam epitaxy of wide bandgap complex oxide semiconductors," J. Mater. Res. **36**, 4846–4864 (2021).

[35] A. J. Schmidt, R. Cheaito, and M. Chiesa, "A frequency-domain thermoreflectance method for the characterization of thermal properties," Rev. Sci. Instrum. **80**, 094901 (2009).

[36] D. G. Cahill *et al.*, "Analysis of heat flow in layered structures for time-domain thermoreflectance," Rev. Sci. Instrum. **75**, 5119 (2004).

[37] A. J. Schmidt, X. Chen, and G. Chen, "Pulse accumulation, radial heat conduction, and anisotropic thermal conductivity in pump-probe transient thermoreflectance," Rev. Sci. Instrum. **79**, 114902 (2008).

[38] G. Alvarez-Escalante, R. Page, R. Hu, H. G. Xing, D. Jena, and Z. Tian, "High thermal conductivity and ultrahigh thermal boundary conductance of homoepitaxial AlN thin films," APL Mater. **10**, 011115 (2022).

[39] G. A. Alvarez, J. Christiansen-Salameh, A. Biswas, A. B. Puthirath, E. Jeong, J. Kwon, J. Lee, T. Gray, R. Vajtai, P. M. Ajayan *et al.*, "Cross-plane thermal conductivity of h-BN thin films grown by pulsed laser deposition," Appl. Phys. Lett. **122**, 232101 (2023).

[40] G. A. Alvarez, J. Casamento, L. Van Deurzen, M. I. Khan, K. Khan, E. Jeong, E. Ahmadi, H. G. Xing, D. Jena, and Z. Tian, "Thermal conductivity enhancement of aluminum scandium nitride grown by molecular beam epitaxy," Mater. Res. Lett. **11**, 1048–1054 (2023).

[41] M. Ritala, M. Leskela, and H. Nalwa, *Handbook of Thin Film Materials: Deposition and Processing of Thin Films* (Academic Press, 2002), Vol. 1, p. 103.

[42] R. Page, J. Casamento, Y. Cho, S. Rouvimov, H. G. Xing, and D. Jena, "Rotationally aligned hexagonal boron nitride on sapphire by high-temperature molecular beam epitaxy," Phys. Rev. Mater. **3**, 064001 (2019).

[43] J. Casamento, J. Wright, R. Chaudhuri, H. G. Xing, and D. Jena, "Molecular beam epitaxial growth of scandium nitride on hexagonal SiC, GaN, and AlN," Appl. Phys. Lett. **115**, 172101 (2019).

[44] M. Henini, *Molecular Beam Epitaxy: From Research to Mass Production* (Elsevier, 2012).

[45] J. Ristić, E. Calleja, S. Fernández-Garrido, L. Cerutti, A. Trampert, U. Jahn, and K. H. Ploog, "On the mechanisms of spontaneous growth of III-nitride nanocolumns by plasma-assisted molecular beam epitaxy," J. Cryst. Growth **310**, 4035–4045 (2008).

[46] W. E. Hoke, A. Torabi, J. J. Mosca, and T. D. Kennedy, "Thermodynamic analysis of cation incorporation during molecular beam epitaxy of nitride films using metal-rich growth conditions," J. Vac. Sci. Technol. B **25**, 978–982 (2007).

[47] D. Zhuang and J. H. Edgar, "Wet etching of GaN, AlN, and SiC: A review," Mater. Sci. Eng. R: Rep. **48**, 1–46 (2005).

[48] M. Bickermann, S. Schmidt, B. Epelbaum, P. Heimann, S. Nagata, and A. Winnacker, "Wet KOH etching of freestanding AlN single crystals," J. Cryst. Growth **300**, 299–307 (2007).

[49] M. Takeuchi, H. Shimizu, R. Kajitani, K. Kawasaki, T. Kinoshita, K. Takada, H. Murakami, Y. Kumagai, A. Koukitu, T. Koyama *et al.*, "Al-and N-polar AlN layers grown on c-plane sapphire substrates by modified flow-modulation MOCVD," J. Cryst. Growth **305**, 360–365 (2007).

[50] Y. Cho, C. S. Chang, K. Lee, M. Gong, K. Nomoto, M. Toita, L. J. Schowalter, D. A. Muller, D. Jena, and H. G. Xing, "Molecular beam homoepitaxy on bulk AlN enabled by aluminum-assisted surface cleaning," Appl. Phys. Lett. **116**, 172106 (2020).

[51] J. Singhal, J. Encomendero, Y. Cho, L. van Deurzen, Z. Zhang, K. Nomoto, M. Toita, H. G. Xing, and D. Jena, "Molecular beam homoepitaxy of N-polar AlN on bulk AlN substrates," AIP Adv. **12**, 095314 (2022).

[52] Z. Zhang, Y. Hayashi, T. Tohei, A. Sakai, V. Protasenko, J. Singhal, H. Miyake, H. G. Xing, D. Jena, and Y. Cho, "Molecular beam homoepitaxy of N-polar AlN: Enabling role of aluminum-assisted surface cleaning," Sci. Adv. **8**, 6408 (2022).

[53] A. W. Searcy and C. E. Myers, "The heat of sublimation of boron and the gaseous species of the boron–boric oxide system," J. Phys. Chem. **61**, 957–960 (1957).

[54] R. E. Honig, *Vapor Pressure Data for the More Common Elements* (David Sarnoff Research Center, 1957).

[55] G. Verhaegen and J. Drowart, "Mass spectrometric determination of the heat of sublimation of boron and of the dissociation energy of B_2," J. Chem. Phys. **37**, 1367–1368 (1962).

[56] L. Vel, G. Demazeau, and J. Etourneau, "Cubic boron nitride: Synthesis, physicochemical properties and applications," Mater. Sci. Eng.: B **10**, 149–164 (1991).

[57] F. R. Corrigan and F. P. Bundy, "Direct transitions among the allotropic forms of boron nitride at high pressures and temperatures," J. Chem. Phys. **63**, 3812–3820 (1975).

[58] X. Li, S. Wang, H. Liu, F. A. Ponce, T. Detchprohm, and R. D. Dupuis, "100-nm thick single-phase wurtzite BAlN films with boron contents over 10%," Phys. Status Solidi B **254**, 1600699 (2017).

[59] M. Imura, Y. Ota, R. G. Banal, M. Liao, Y. Nakayama, M. Takeguchi, and Y. Koide, "Effect of boron incorporation on structural and optical properties of AlN layers grown by metal-organic vapor phase epitaxy," Phys. Status Solidi A **215**, 1800282 (2018).

[60] J. Sarker, T. B. Tran, F. AlQatari, C.-H. Liao, X. Li, and B. Mazumder, "Nanoscale compositional analysis of wurtzite BAlN thin film using atom probe tomography," Appl. Phys. Lett. **117**, 232103 (2020).

[61] P. Vuong, A. Mballo, S. Sundaram, G. Patriarche, Y. Halfaya, S. Karrakchou, A. Srivastava, K. Krishnan, N. Sama, T. Ayari *et al.*, "Single crystalline boron rich B(Al)N alloys grown by MOVPE," Appl. Phys. Lett. **116**, 042101 (2020).

[62] C. Milne, T. Biswas, and A. K. Singh, "Ab initio prediction of ultra-wide band gap $B_xAl_{1-x}N$ materials," Adv. Electron. Mater. **9**, 2201197 (2023).

[63] A. N. Mariano and R. E. Hanneman, "Crystallographic polarity of ZnO crystals," J. Appl. Phys. **34**, 384–388 (1963).

[64] I. Vurgaftman and J. R. Meyer, "Band parameters for nitrogen-containing semiconductors," J. Appl. Phys. **94**, 3675–3696 (2003).

[65] T. Matsuoka, H. Okamoto, M. Nakao, H. Harima, and E. Kurimoto, "Optical bandgap energy of wurtzite InN," Appl. Phys. Lett. **81**, 1246–1248 (2002).

[66] D. A. Evans, A. G. McGlynn, B. M. Towlson, M. Gunn, D. Jones, T. E. Jenkins, R. Winter, and N. R. J. Poolton, "Determination of the optical band-gap energy of cubic and hexagonal boron nitride using luminescence excitation spectroscopy," J. Phys.: Condens. Matter **20**, 075233 (2008).

[67] F. Yun, M. A. Reshchikov, L. He, T. King, H. Morkoç, S. W. Novak, and L. Wei, "Energy band bowing parameter in Al_xGa_{1-x}Nalloys," J. Appl. Phys. **92**, 4837–4839 (2002).

[68] M. Baeumler, Y. Lu, N. Kurz, L. Kirste, M. Prescher, T. Christoph, J. Wagner, A. Žukauskaitė, and O. Ambacher, "Optical constants and band gap of wurtzite $Al_{1-x}Sc_xN/Al_2O_3$ prepared by magnetron sputter epitaxy for scandium concentrations up to $x = 0.41$," J. Appl. Phys. **126**, 045715 (2019).

[69] T. Nguyen, K. Nomoto, W. Zhao, C. Savant, X. Xing, and D. Jena, "Strain-balanced AlScN/GaN HEMTs with ft/fmax of 173/321 GHz," in *2024 International Electron Devices Meeting (IEDM)* (IEEE, 2024), pp. 9.5.1–9.5.4.

[70] C. P. Savant, A. Verma, T.-S. Nguyen, L. van Deurzen, Y.-H. Chen, Z. He, S. S. Rezaie, J. Gollwitzer, B. Gregory, S. Sarker *et al.*, "Self-activated epitaxial growth of ScN films from molecular nitrogen at low temperatures," APL Mater. **12**, 111108 (2024).

[71] R. Pelá, C. Caetano, M. Marques, L. Ferreira, J. Furthmüller, and L. Teles, "Accurate band gaps of AlGaN, InGaN, and AlInN alloys calculations based on LDA-1/2 approach," Appl. Phys. Lett. **98**, 151907 (2011).

[72] Y. Hasegawa, T. Akiyama, A.-M. Pradipto, K. Nakamura, and T. Ito, "Theoretical investigations on the structural stability and miscibility in BAlN and BGaN alloys: Bond-order interatomic potential calculations," Jpn. J. Appl. Phys. **58**, SCCB21 (2019).

[73] K. Hirata, K. Shobu, H. Yamada, M. Uehara, S. A. Anggraini, and M. Akiyama, "Thermodynamic assessment of the Al–Sc–N ternary system and phase-separated region of the strained wurtzite phase," J. Eur. Ceram. Soc. **40**, 5410–5422 (2020).

[74] S. Satoh, K. Ohtaka, T. Shimatsu, and S. Tanaka, "Crystal structure deformation and phase transition of AlScN thin films in whole Sc concentration range," J. Appl. Phys. **132**, 025103 (2022).

[75] A. J. E. Rowberg, S. Mu, M. W. Swift, and C. G. Van de Walle, "Structural, electronic, and polarization properties of YN and LaN," Phys. Rev. Mater. **5**, 094602 (2021).

[76] M. J. Slomski, "Thermal conductivity of group-III nitrides and oxides," Ph.D. thesis (North Carolina State University, 2017).

[77] A. Filatova-Zalewska, Z. Litwicki, T. Suski, and A. Jeżowski, "Thermal conductivity of thin films of gallium nitride, doped with aluminium, measured with 3ω method," Solid State Sci. **101**, 106105 (2020).

[78] S. Adachi, "Lattice thermal conductivity of group-IV and III-V semiconductor alloys," J. Appl. Phys. **102**, 063502 (2007).

[79] S. Vitanov, "Simulation of high electron mobility transistors," Ph.D. thesis (Technische Universität, Wien, 2010).

[80] B. Pantha, R. Dahal, J. Li, J. Lin, H. Jiang, and G. Pomrenke, "Thermoelectric properties of $In_xGa_{1-x}N$ alloys," Appl. Phys. Lett. **92**, 042112 (2008).

[81] S. Yamaguchi, R. Izaki, K.-i. Yamagiwa, K. Taki, Y. Iwamura, and A. Yamamoto, "Thermal diffusivity and thermoelectric figure of merit of $Al_{1-x}In_xN$ prepared by reactive radio-frequency sputtering," Appl. Phys. Lett. **83**, 5398–5400 (2003).